applied sciences

MDPI

Article

An Improved Ground Moving Target Parameter Estimation and Imaging Method for Multichannel High Resolution SAR

Qinghai Dong [1,2], Bingnan Wang [1,*], Maosheng Xiang [1,2], Zekun Jiao [1], Zhongbin Wang [1,2] and Chong Song [1,2]

1 National Key Laboratory of Microwave Imaging Technology, Aerospace Information Research Institute, Chinese Academy of Sciences, Beijing 100094, China; dongqh@aircas.ac.cn (Q.D.); xms@mail.ie.ac.cn (M.X.); jiaozk@aircas.ac.cn (Z.J.); wangzhongbin17@mails.ucas.ac.cn (Z.W.); songchong18@mails.ucas.edu.cn (C.S.)

2 School of Electronic, Electrical and Communication Engineering, University of Chinese Academy of Sciences, Beijing 100094, China

* Correspondence: wbn@mail.ie.ac.cn; Tel.: +86-010-5888-7023

Abstract: With increasing demands from both military and civilian applications, ground moving-target imaging is becoming one of the important research topics for high-resolution SAR systems. However, the existing moving-target imaging methods are not suitable for high-resolution SAR because of their low parameter estimation accuracy and high computational complexity. To solve the problem, an improved ground moving-target parameter estimation and imaging method is proposed. First, the third-order phase model of the uniformly accelerated target signal is constructed, and the Hough transform and the second-order Keystone transform (SOKT) are used to correct the range cell migration into one range cell to achieve target coherent accumulation. Secondly, a delayed cross-correlation function (DCCF) is constructed to reduce the order of the range migration phase response in the slow time domain, and the coupling degree between the cross-correlation peak position and the range migration is reduced, so that the obtained DCCF has a higher gain, which ensures the accuracy of parameter estimation. Parameter estimation is simplified to peak detection by the Shift-And-Correlation (SAC) algorithm and two-dimensional Fourier transform (2D-FFT), avoiding parameter search. Compared with the existing methods, the proposed method has better focusing effect and lower computational complexity. Finally, simulation and measured data are given to verify the effectiveness of the proposed method.

Keywords: Synthetic Aperture Radar (SAR); ground moving-target imaging; Hough transform; second-order Keystone (SOKT); Shift-And-Correlation (SAC)

check for updates

Citation: Dong, Q.; Wang, B.; Xiang, M.; Jiao,Z.; Wang, Z.; Song, C. An Improved Ground Moving Target Parameter Estimation and Imaging Method for Multichannel High Resolution SAR. *Appl. Sci.* **2022**, *12*, 4934. https://doi.org/10.3390/app12104934

Academic Editor: Amerigo Capria

Received: 18 March 2022
Accepted: 11 May 2022
Published: 13 May 2022

1. Introduction

Synthetic Aperture Radar (SAR) is widely used in military and civilian fields due to its high-resolution imaging of a target, its large coverage, and its all-weather capability [1–3]. Ground moving-target detection based on multi-channel SAR plays an increasingly important role in battlefield surveillance, traffic surveillance and other applications [4–6]. The conventional SAR imaging algorithm is designed for stationary targets in the observation scene, which uses motion parameters and the slant range history between the platform and the target to obtain focused imaging. Because the motion parameters of the target are not known, the moving target is defocused in SAR images and deviates from its real position, which makes it difficult to detect, identify and locate the target. Therefore, in order to obtain a well-focused image of a moving target, the motion parameters of the target must be accurately estimated.

In high-resolution SAR images, moving-target refocusing can not only improve the signal-to-noise ratio of the target, but also the focused target can reflect its structure and attitude to a certain extent, which is conducive to target recognition and classification. Therefore, moving-target imaging has become one of the hotspots of SAR-GMTI research.

With the improvement of SAR resolution and the continuous increase of synthetic aperture time, the high-order range migration caused by target motion cannot be ignored, which will increase the difficulty of range cell migration correction (RCMC) and parameter estimation. There are two problems in the existing moving-target parameter estimation. (1) Ignoring the range migration caused by high-order terms leads to poor parameter estimation accuracy [7,8]. For high-resolution SAR systems, ignoring the high-order terms of range migration will cause residual range migration, resulting in a large parameter estimation error. For example, reference [7] did not consider the third-order term when performing the instantaneous slant-range expansion. Although reference [8,9] constructed a third-order slant range model, the influence of the third-order range migration on the cross-correlation function was ignored in the parameter estimation; as a result, the energy of DCCF could not be gathered into the same range cell. (2) In order to pursue the accuracy of parameter estimation, the method of parameter traversal is used to search for the optimal value, which increases the computational complexity [10–12]. For example, reference [13] uses the Chirp Scaling Algorithm (CSA) to image moving targets, and reference [8] uses SOKT, Radon, Fourier transform and parameter search to obtain focused moving targets. Reference [14] traverses all range frequency points in the range frequency–azimuth-time domain and takes the average value as the estimation result. Reference [15] uses the convolutional neural network for moving-target imaging, which requires a large number of training data sets.

Reference [9] proposed an algorithm called keystone transform and coherently integrated cubic phase function (KT-CICPF). The DCCF of KT-CICPF is constructed before RCMC. In the DCCF constructed by KT-CICPF, the energy of the moving target is dispersed into multiple range cells, resulting in defocusing of the peak of the constructed parameter estimation plane. In addition, when the RCMC is performed, the movement amount of the third-order term is ignored, resulting in parameter estimation errors.

Aiming at the above two problems, this paper proposes an improved moving-target imaging method based on high-order parameter estimation. Firstly, the Hough transform and the SOKT are used to correct the range migration to improve the coherent accumulation gain of the target. Secondly, the DCCF is constructed to reduce the order of the range migration phase response in the slow-time domain. Different from the existing methods [10,11,13,14,16,17], the proposed method constructs the DCCF after the RCMC and compensates the residual range migration with the estimated third-order terms. The proposed method can obtain the DCCF with a higher integral gain, which ensures the performance of parameter estimation. In addition, the proposed method simplifies parameter estimation to peak detection through the SAC algorithm and 2D-FFT, avoiding parameter search.

In this paper, focus imaging is performed on the raw data. So, clutter suppression, target detection and target signal extraction are necessary before refocusing the moving target. After clutter suppression and target detection, the background is sufficiently uncluttered. The proposed method can be summed up five steps. Step I: Clutter suppression and target detection based on multi-channel and target signal extraction. Step II: The RCMC is realized by Hough transform and SOKT. Step III: Constructing DCCF to reduce the third-order phase in the slow-time domain to second-order; then the parameter estimation is converted into peak detection with the SAC algorithm and 2D-FFT, which simplify the parameter estimation process. Step IV: The moving-target focusing imaging is performed by the estimated third-order phase coefficient. Finally, based on the estimated parameters, the target is relocated.

The remainder of this paper is structured as follows. In Section 2, the third-order signal model of the uniformly accelerated target is constructed. In Section 3, an improved ground moving-target parameter estimation and imaging method for multichannel high-resolution SAR is proposed. In Section 4, the imaging process of a moving target based on the measured data is given. In Section 5, the effectiveness of the proposed method is verified by simulation and measured data. In Section 6, the proposed method is summarized and discussed.

2. Signal Model

In the two-dimensional slant plane, the observation geometry between the side-looking airborne SAR platform with velocity v (x-axis direction) and a ground moving target is shown in Figure 1. At the azimuth time $t_a = 0$, there is a target moving with uniform acceleration at the same azimuth position of the platform, and the coordinate position of the moving target is $P_0 = (0, R_0)^T$, where T stands for vector transposition. This paper assumes that the target is accelerated uniformly. Its initial velocity and acceleration vectors along-track and cross-track are $V_t = [v_x, v_r]^T$ and $a_t = [a_x, a_r,]^T$, respectively. After a period of time, the target moves to P_t, and the instantaneous coordinates of the moving target can be expressed as

$$P_t = P_0 + V_t t_a + \frac{1}{2} a_t t_a^2 = [v_x t_a + \frac{1}{2} a_x t_a^2, R_0 + v_r t_a + \frac{1}{2} a_r t_a^2]^T \tag{1}$$

According to the geometric relationship between the radar and the moving target, the instantaneous range from the antenna phase center to the moving target can be written as [2]

$$R(t_a) = \sqrt{\left(v t_a - v_{x0} t_a - \frac{1}{2} a_x t_a^2\right)^2 + \left(R_0 - v_r t_a - \frac{1}{2} a_r t_a^2\right)^2} \tag{2}$$

For high-resolution SAR systems, due to the existence of target acceleration, the instantaneous range $R(t_a)$ can be expanded to the third-order term based on the Taylor series expansion. Ignoring the fourth and above higher orders, we can obtain [8,14,18,19]

$$R(t_a) \approx R_0 + a_1 t_a + a_2 t_a^2 + a_3 t_a^3 \tag{3}$$

where $a_1 = -v_r$, $a_2 = \frac{(v - v_x)^2}{2R_0} - \frac{a_r}{2}$, $a_3 = \frac{v_r (v - v_x)^2}{2R_0^2} + \frac{a_x (v_x - v)}{2R_0}$ are the unknown parameters that need to be estimated.

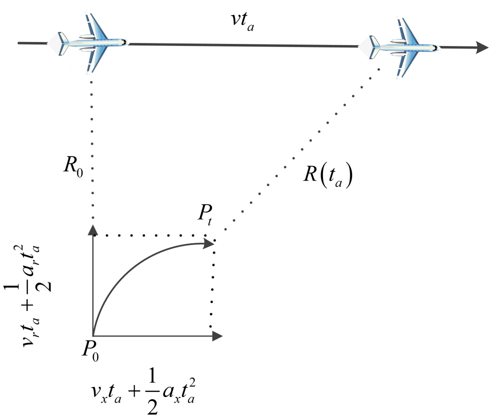

Figure 1. The observation geometry between airborne SAR platform and a moving target.

The system transmits a linear frequency modulation signal, and, after pulse compression in range direction, the received baseband signal can be expressed as [20]

$$S_1(t_r, t_a) = A w_a(t_a) sinc\left[B\left(t_r - \frac{2R(t_a)}{c}\right)\right] \exp\left\{-j\frac{4\pi f_c R(t_a)}{c}\right\} \tag{4}$$

A is the product of the complex reflectivity and the range compression gain of the target, $w_a(t_a) = rect\left(\frac{t_a}{T_s}\right)$ represents the azimuth window function, $sinc(\cdot)$ represents the point spread function, and B, c and f_c represent the bandwidth of the transmitted signal, the speed of light and the signal carrier frequency, respectively.

By calculating the first and second derivatives of the phase of Equation (4), the Doppler shift and the instantaneous azimuth modulation frequency of the moving target can be written down, respectively [10]:

$$f_{dc} = \frac{2v_r}{\lambda}, \mathrm{Ka} = \frac{4(a_2 + 3a_3t_a)}{\lambda} \tag{5}$$

where $\lambda = c/f_c$ represents the wavelength of the signal. The received signal in the range-frequency domain can be expressed as [9]

$$\begin{aligned} S_1(f_r, t_a) &= Aw_a(t_a)rect\left(\frac{f_r}{B}\right)\exp\left\{-j\frac{4\pi(f_r + f_c)}{c}R(t_a)\right\} \\ &= Aw_a(t_a)rect\left(\frac{f_r}{B}\right)\exp\left\{-j\frac{4\pi(f_r + f_c)}{c}\left(R_0 + a_1t_a + a_2t_a^2 + a_3t_a^3\right)\right\} \end{aligned} \tag{6}$$

It can be seen from Equation (5) that the Doppler frequency rate of the moving target is not only affected by the target motion, but is also time-varying. Therefore, it is difficult to obtain a good focusing effect only using second-order parameter estimation.

For a moving target, a_1 causes the range walk and Doppler center shift, parameters a_2 and a_3 produce range curvature and Doppler spectral broadening. In a synthetic aperture time T_s, the range migration spans multiple range cells. The range walk and range curvature caused by the target movement can be written, respectively, as [8,21]:

$$R_{walk} = a_1T_s \tag{7}$$

$$R_{cure} = a_2T_s^2 + a_3T_s^3 \tag{8}$$

When the range migration is greater than half the range cell interval, the range migration must be corrected to achieve azimuth focusing [22]. For high-resolution SAR systems, the range migration generated by Equations (7) and (8) spans multiple range cells. Since the target motion parameters are unknown, the use of stationary target parameters for imaging will result in a mismatch between residual range migration and azimuth compression, which will eventually lead to defocusing of moving targets in the SAR image and deviation from the true position of the target.

3. The Proposed Method

In this section, an improved ground moving-target parameter estimation and imaging method for multichannel high-resolution SAR is proposed. Firstly, the Hough and SOKT are used to correct the range migration to achieve target coherent accumulation. Secondly, DCCF is constructed to reduce the order of the range migration phase response in the slow time domain. Then, the parameter estimation is converted into peak detection with the SAC algorithm and 2D-FFT, which simplifies the parameter estimation process. Finally, the moving-target focusing imaging and relocation are performed based on the estimated parameter.

3.1. Rcmc Based on Hough-SOKT

When the squint angle or the radial velocity of the target is large, the Doppler center shift is large, and the range walk is usually larger than the range curvature. In order to reduce the coupling effect of range walk and range curvature, the first-order term in Equation (3) must be corrected to remove the main component in the range migration. In the two-dimensional time domain, the range walk appears as an oblique line in the image, and its slope is proportional to the radial velocity of the target [23]. Therefore, Hough transform can be used to transform the estimation of the range walk into the estimation of walk inclination to realize range walk correction. In the two-dimensional time domain, Hough transform uses the trajectory information of the moving target to estimate parameters, so there is no need to worry about the influence of Doppler spectrum ambiguity on the estimation result of the Doppler centroid.

The schematic diagram of the two-dimensional time domain Hough transform is shown in Figure 2, where θ is the angle between the target's moving direction and the azimuth direction, and the Hough transforms a straight line in the coordinate space into a peak point in the parameter space (ρ, θ). The inclination of the line can be estimated by detecting the position of the peak in the transform domain.

The relationship between the estimated value of the radial velocity v_r and θ can be written as [23]

$$\widehat{v_r} = \frac{c \cdot PRF}{2f_s} \tan(\theta) \tag{9}$$

where PRF and f_s denote the azimuth and range sampling frequencies, respectively.

The estimated Doppler center is $f_{ref} = {}^{2\widehat{v_r}}/_{\lambda}$. In the azimuth-time domain and range-frequency domain, the required phase compensation for the range walk in Equation (6) can be written as [10,24]

$$H_{fdc}(f_r, t_a) = \exp\left\{-j2\pi f_{ref} \frac{f_r + f_c}{f_c} t_a\right\} \tag{10}$$

For Equation (6), error in v_r leads to the residual of the range walk after correction. Therefore, the signal of the moving target after range walk correction can be expressed as

$$S_2(f_r, t_a) = Aw_a(t_a)rect\left(\frac{f_r}{B}\right) \exp\left\{-j\frac{4\pi(f_r + f_c)}{c}\left(R_0 + a'_1 t_a + a_2 t_a^2 + a_3 t_a^3\right)\right\} \tag{11}$$

where $a_1' = a_1 + \widehat{v_r}$ is the residual first-order term after range walk correction.

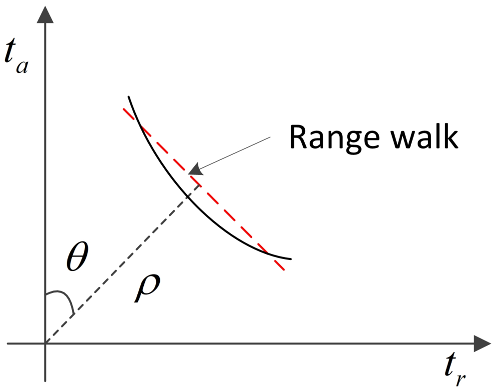

Figure 2. Hough transform schematic (the red line is the estimated range walk, and the black curve is the real range migration).

After the range walk correction, the residual amount of the first-order term is small, and the main component of the residual range migration is the range curvature. The SOKT is used to correct the range curvature [10,19,25]. The new azimuth-time variable is denoted by t_m, and the azimuth-time scale transformation relation is as follows [8]

$$t_a = \sqrt{\frac{f_c}{f_r + f_c}} \cdot t_m \tag{12}$$

Substituting Equation (12) into Equation (11), the azimuth-time domain and range-frequency domain signal after the SOKT is

$$S_3(f_r, t_m) = Aw_a(t_m)rect\left(\frac{f_r}{B}\right) \exp\{-j\Phi_1(f_r, t_m)\} \tag{13}$$

The expression of $\Phi_1(f_r, t_m)$ in the above equation is written as

$$\begin{aligned}\Phi_1(f_r, t_m) = &\frac{4\pi(f_r + f_c)}{c}R_0 + \frac{4\pi}{c}\sqrt{f_c(f_r + f_c)}a'_1 t_m \\ &+ \frac{4\pi f_c}{c}a_2 t_m^2 + \frac{4\pi f_c}{c}\sqrt{\frac{f_c}{f_c + f_r}}a_3 t_m^3\end{aligned} \tag{14}$$

In the range-frequency domain and azimuth-time domain, the coupling between the quadratic term t_m^2 and f_r has been removed after the SOKT, indicating that the range curvature has been corrected.

Generally, the SAR systems satisfies $f_r \ll f_c$, and there is an approximate relationship [19]

$$\begin{cases}\sqrt{f_c(f_r + f_c)} \approx \left(\frac{1}{2}f_r + f_c\right) \\ \sqrt{\frac{f_c}{f_c + f_r}} \approx \left(1 - \frac{f_r}{2f_c}\right)\end{cases} \tag{15}$$

Substituting Equation (15) into Equation (14) yields

$$\begin{aligned}\Phi_1(f_r, t_m) \approx &\frac{4\pi(f_r + f_c)}{c}R_0 + \frac{4\pi f_c}{c}a'_1 t_m + \frac{2\pi f_r}{c}a'_1 t_m \\ &+ \frac{4\pi f_c}{c}a_2 t_m^2 + \frac{4\pi f_c}{c}a_3 t_m^3 - \frac{2\pi f_r}{c}a_3 t_m^3\end{aligned} \tag{16}$$

Transforming Equation (13) into the two-dimensional time domain, the range–azimuth two-dimensional time domain signal after the SOKT can be obtained as

$$S_3(t_r, t_m) = Aw_a(t_m)sinc\left[B\left(t_r - \frac{2R_0 + a'_1 t_m - a_3 t_m^3}{c}\right)\right]\exp\{-j\Phi_1(t_r, t_m)\} \tag{17}$$

The expression of $\Phi_1(t_r, t_m)$ in the above equation is written

$$\Phi_1(t_r, t_m) = \frac{4\pi f_c}{c}\left(R_0 + a'_1 t_m + a_2 t_m^2 + a_3 t_m^3\right) \tag{18}$$

Typically, the range migration due to the cubic term is less than one range cell. Moreover, the residual term of the first-order corrected by Hough transform is small. After Hough and SOKT processing, most of the target's energy is concentrated into a range cell.

3.2. Construction of DCCF

In this paper, DCCF is constructed in the range-frequency domain and the azimuth-time domain to reduce envelope shift and the order of phase response in the slow-time domain. Thereby, the accuracy of range migration correction is improved and the estimation of target motion parameters is simplified. Different from the method in reference [19], in this paper, the DCCF is constructed after RCMC, which reduces the coupling degree between the peak position of the DCCF and the target range migration. The obtained cross-correlation function has higher gain, which ensures the performance of parameter estimation.

After the processing in Section 3.1, although the third and sixth items in Equation (16) still have the signal envelope shift caused by the residual range–azimuth coupling, the impact is small. The energy of the moving target is basically corrected to within a range cell. For Equation (13), the DCCF constructed in the range-frequency domain and azimuth-time domain is as follows [10,25]

$$\begin{aligned} S_4(f_r,t_m) &= S_3(f_r,t_m)S_3^*(f_r,t_m-t_0) \\ &= |A|^2 w_a(t_m) w_a(t_m-t_0) rect^2\left(\frac{f_r}{B}\right)\exp\{-j\Delta\Phi_1(f_r,t_m)\} \end{aligned} \tag{19}$$

where t_0 denotes the fixed delay given by $T_s/4$ [10,25].

By combining Equations (13) and (19), the range cell migration factor concerning a_3 in $S_4(f_r,t_m)$ can be obtained. It can be written as

$$H_0(f_r,t_m) = \exp\left\{j\frac{4\pi}{\lambda}\sqrt{\frac{f_c}{f_c+f_r}}a_3\left(t_0^3+3t_0t_m^2-3t_0^2t_m\right)\right\} \tag{20}$$

The range cell migration caused by a_3 will be compensated in Equation (30). Substituting Equation (16) into Equation (19), we can obtain the last factor of Equation (19) as

$$\begin{aligned} H_1(f_r,t_m,t_0) &= \exp\{-j\Delta\Phi_1(f_r,t_m)\} \\ &\approx \exp\left\{-j\frac{4\pi f_c}{c}\left({a'}_1t_0-a_2t_0^2+a_3t_0^3\right)\right\} \\ &\quad \times \exp\left\{-j\frac{4\pi f_c}{c}\left(2a_2t_0-3a_3t_0^2\right)t_m\right\} \times \exp\left\{-j\frac{12\pi f_c}{c}a_3t_0t_m^2\right\} \\ &\quad \times \exp\left\{-j\frac{2\pi f_r}{c}\left({a'}_1t_0-a_3t_0^3\right)\right\} \times \exp\left\{j\frac{6\pi f_r}{c}a_3\left(t_0t_m^2-t_0^2t_m\right)\right\} \end{aligned} \tag{21}$$

The fifth term in $H_1(f_r,t_m,t_0)$ still has range–azimuth coupling, which corresponds to the residual migration after range migration correction.

Substituting Equation (21) into (19), and performing the IFFT in the range dimension, we can obtain

$$\begin{aligned} &S_4(t_r,t_m) \\ &= |A|^2 w_a(t_m)w_a(t_m-t_0)sinc\left[B\left(t_r-\frac{{a'}_1t_0-a_3t_0^3}{c}+\frac{3a_3\left(t_0t_m^2-t_0^2t_m\right)}{c}\right)\right] \\ &\quad \times \exp\left\{-j\frac{4\pi f_c}{c}\left[\left(2a_2t_0-3a_3t_0^2\right)t_m+3a_3t_0t_m^2\right]\right\} \end{aligned} \tag{22}$$

The residual range migration $\Delta R = \left|3a_3\left(t_0t_m^2-t_0^2t_m\right)\right|$ is generally less than a range cell and can be ignored (we will use Equation (30) to compensate for the approximation error here). Therefore, the two-dimensional time domain cross-correlation function can be obtained as

$$\begin{aligned} &S_4(t_r,t_m) \\ &\approx |A|^2 w_a(t_m)w_a(t_m-t_0)sinc\left[B\left(t_r-\frac{{a'}_1t_0-a_3t_0^3}{c}\right)\right] \\ &\quad \times \exp\left\{-j\frac{4\pi f_c}{c}\left[\left({a'}_1t_0-a_2t_0^2+a_3t_0^3\right)+\left(2a_2t_0-3a_3t_0^2\right)t_m+3a_3t_0t_m^2\right]\right\} \\ &= \sigma(t_m)sinc\left[B\left(t_r-\frac{{a'}_1t_0-a_3t_0^3}{c}\right)\right]\exp\left\{-j\frac{4\pi f_c}{c}\left[\left(2a_2t_0-3a_3t_0^2\right)t_m+3a_3t_0t_m^2\right]\right\} \end{aligned} \tag{23}$$

where

$$\begin{aligned} \sigma(t_m) &= rect\left(\frac{t_m}{T_s}\right)rect\left(\frac{t_m-t_0}{T_s}\right)|A|^2\exp\left\{-j\frac{4\pi f_c}{c}\left[\left({a'}_1t_0-a_2t_0^2+a_3t_0^3\right)\right]\right\} \\ &= \begin{cases} |A|^2\exp\left\{-j\frac{4\pi f_c}{c}\left[\left({a'}_1t_0-a_2t_0^2+a_3t_0^3\right)\right]\right\}, -\frac{T_s}{2}+t_0<t_m<\frac{T_s}{2} \\ 0\ ,\ else \end{cases} \end{aligned}$$

It can be seen from Equation (23) that the energy of the moving target is concentrated into a range cell after the above processing, and the order of the range migration phase response in the slow-time domain is reduced. The purpose of reducing the complexity of parameter estimation and improving the accuracy of parameter estimation is achieved.

The signal of the range cell where the peak of DCCF is located is a linear frequency modulation signal in the slow-time domain. It can be written as

$$S_5(t_m) = S_4(F_0, t_m) = \omega \exp\left\{ j2\pi \left(F_1 t_m + 0.5 F_2 t_m^2 \right) \right\}, -\frac{T_s}{2} + t_0 < t_m < \frac{T_s}{2} \tag{24}$$

where ω is the envelope of the signal. For given system parameters, ω is a constant. $F_0 = \frac{a'_1 t_0 - a_3 t_0^3}{c}$, $F_1 = -\frac{4a_2 t_0 - 6a_3 t_0^2}{\lambda}$ and $F_2 = -\frac{12 a_3 t_0}{\lambda}$ correspond to the range gate where $S_5(t_m)$ is located, the Doppler center and the azimuth modulation frequency rate, respectively. The motion parameters of the target can be obtained by estimating F_0, F_1 and F_2.

3.3. Parameter Estimation Based on SAC Algorithm and 2D-FFT

In this paper, the DCCF calculation is performed after RCMC, which reduces the coupling degree between the cross-correlation peak position and the target. Therefore, the SAC algorithm is more suitable for estimating the azimuth modulation frequency of $S_5(t_m)$ [26].

Based on the above analysis, we know that ω in Equation (24) is a constant. The amplitude factor of $S_5(t_m)$ has been neglected since it has no impact on the peak position of $S_{SAC}(t_m)$. Let us perform FFT on Equation (24), then move the center of the Doppler spectrum to zero frequency. According to the principle of stationary phase, the azimuth spectrum can be simplified as [27,28]

$$S_5(f_m) = FFT[S_5(t_m)] = \exp\left\{ -j\pi \frac{f_m^2}{F_2} \right\}, -\frac{B_a}{2} \leqslant f_m \leqslant \frac{B_a}{2} \tag{25}$$

where f_m represents the Doppler frequency and B_a represents the Doppler bandwidth.

The principle of the SAC algorithm is shown in Figure 3. It can be seen that the SAC algorithm can estimate the value of F_2 without iteration. The Doppler spectrum of the signal is divided into left and right sub-bands, and then the cross-correlation function after sub-band translation is obtained. The cross-correlation peak position can be used to estimate the Doppler modulation frequency. The spectrum of $S_5(f_m)$ is divided into left and right parts. The left and right spectra obtained by shifting $+\Delta f_m$ and $-\Delta f_m$, respectively, can be expressed as [26]

$$\begin{cases} S_{5L}(f_m) = \exp\left\{ -j\pi \dfrac{(f_m - \Delta f_m)^2}{F_2} \right\}, -\dfrac{B_a}{2} + \Delta f_m \leqslant f_m \leqslant \Delta f_m \\ S_{5R}(f_m) = \exp\left\{ -j\pi \dfrac{(f_m + \Delta f_m)^2}{F_2} \right\}, -\Delta f_m \leqslant f_m \leqslant \dfrac{B_a}{2} - \Delta f_m \end{cases} \tag{26}$$

where Δf_m is given by $\frac{B_a}{4}$ [26].

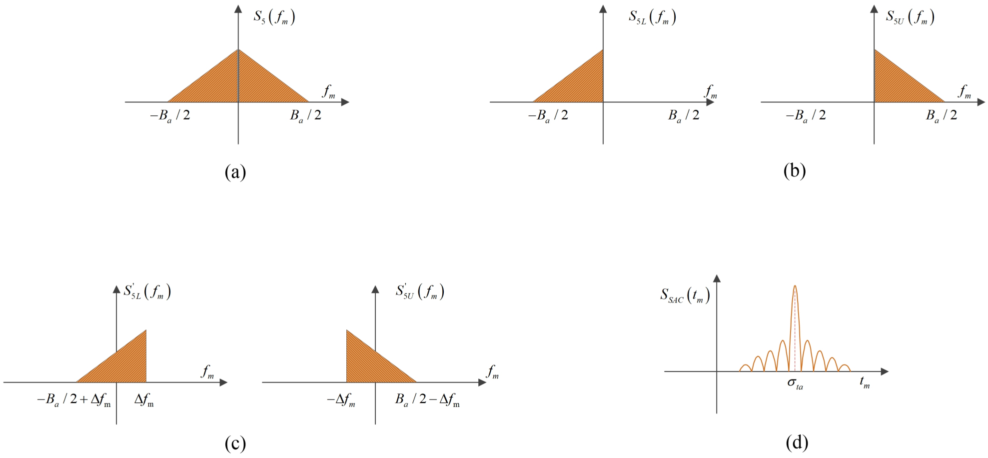

Figure 3. The principle of the SAC algorithm. (**a**) Spectrum. (**b**) Spectrum division. (**c**) Spectrum shifting. (**d**) Signal cross correlation.

A single-frequency signal can be obtained by Equation (27).

$$S_{SAC}(f_m) = S_{5L}(f_m)S_{5R}^*(f_m) = \exp\left(j2\pi\frac{2\Delta f_m}{F_2}f_m\right) \tag{27}$$

We can obtain $S_{SAC}(t_m)$ by performing IFFT on $S_{SAC}(f_m)$. The peak of $S_{SAC}(t_m)$ will appear at σ_{tm}. The estimated value of a_3 can be obtained with Equation (28).

$$\sigma_{tm} = \frac{2\Delta f_m}{F_2},\ a_3 = -\frac{\Delta f_m \lambda}{3\sigma_{tm}t_0} \tag{28}$$

It should be noted that when using Equation (24) to extract the slow time-domain chirp signal, the range-frequency domain and azimuth-time domain coupling term (the fifth term) in Equation (21) is ignored, resulting in a residual range migration. Therefore, the estimated value of a_3 is used to construct a phase factor to compensate for the ignored range migration in Equation (24). According to Equation (20), the constructed phase compensation factor can be written as

$$H_2(f_r,t_m) = \exp\left\{j\frac{4\pi}{\lambda}\sqrt{\frac{f_c}{f_c+f_r}}\widehat{a_3}\left(t_0^3+3t_0t_m^2-3t_0^2t_m\right)\right\} \tag{29}$$

Multiplying Equations (19) and (29), the compensated signal can be obtained as

$$\begin{aligned} S_6(f_r,t_m) &= S_4(f_r,t_m)H_2(f_r,t_m) \\ &= w_a(t_m)w_a(t_m-t_0)rect^2\left(\frac{f_r}{B}\right)\ \exp\{-j2\pi F_0 f_r\}\exp\{j2\pi F_1 t_m\} \end{aligned} \tag{30}$$

The energy of $S_6(f_r,t_m)$ can be accumulated by performing range IFFT and azimuth FFT on the compensated $S_6(f_r,t_m)$. The range-time domain and azimuth-Doppler domain signal obtained can be written as [7]

$$\begin{aligned} S_6(t_r,f_m) &= FFT_{t_m}\left\{IFFT_{f_r}[S_6(f_r,t_m)]\right\} \\ &= A\sigma_0(t_r-F_0)\sigma_0(f_m-F_1) \end{aligned} \tag{31}$$

where $\delta_0(\cdot)$ denotes the Dirac delta function.

The peak positions of Equation (31) correspond to F_0 and F_1, respectively. Therefore, the values of F_0 and F_1 can be estimated by performing peak detection on the data obtained by Equation (31), thereby estimating the values of a_1' and a_2.

In the range direction, F_0 represents the sampling time corresponding to the peak position, and the sampling interval $R_{bin} = {}^{c}/_{2f_s}$ in the range-time domain is generally at the centimeter level or larger. The error of a_1' estimated directly by Equation (31) may be large. Therefore, zero-padding at the end of the data increases the Fourier transform length, when the range dimension inverse Fourier transform is performed, thereby improving the parameter estimation accuracy.

So far, three unknown parameters, a_1, a_2 and a_3 in Equation (6), have been estimated, and their estimated values are $\widehat{a_1}$, $\widehat{a_2}$ and $\widehat{a_3}$, respectively.

3.4. Focused Imaging and Relocation

After the motion parameter estimation is completed, the focused imaging of moving objects can be achieved through two steps of RCMC and matched filtering in the azimuth direction. For Equation (6), the range migration phase compensation factor constructed from the estimates of a_1, a_2 and a_3 can be written as [10]

$$H_{rcmc}(f_r, t_a) = Aw_a(t_a)rect\left(\frac{f_r}{B}\right)\exp\left\{j\frac{4\pi f_r}{c}\left(a_1 t_a + a_3 t_a^2 + a_3 t_a^3\right)\right\} \tag{32}$$

By combining Equations (6) and (32), the range-frequency domain and azimuth-time domain signal after the RCMC can be written as

$$\begin{aligned} S_7(f_r, t_a) &= S_1(f_r, t_a)H_{rcmc}(f_r, t_a) \\ &= Aw_a(t_a)rect\left(\frac{f_r}{B}\right)\exp\left\{-j\frac{4\pi f_r R_0}{c}\right\} \\ &\quad \times \exp\left\{-j\frac{4\pi f_c}{c}\left(R_0 + a_1 t_a + a_2 t_a^2 + a_3 t_a^3\right)\right\} \end{aligned} \tag{33}$$

Performing IFFT in the range direction on Equation (33), the two-dimensional time domain signal after RCMC can be obtained as

$$\begin{aligned} S_7(t_r, t_a) &= Aw_a(t_a)sinc\left[B\left(t_r - \frac{2R_0}{c}\right)\right] \\ &\quad \times \exp\left\{-j\frac{4\pi f_c}{c}\left(R_0 + a_1 t_a + a_2 t_a^2 + a_3 t_a^3\right)\right\} \end{aligned} \tag{34}$$

According to the signal obtained by Equation (34), an azimuth matched filter is constructed to perform azimuth focusing and positioning. The azimuth matched filter can be obtained with Equation (35).

$$H_{match}(t_r, f_a) = FFT_{t_a}\left\{w_a(t_a)\exp\left\{-j\frac{4\pi f_c}{c}\left(a_1 t_a + a_2 t_a^2 + a_3 t_a^3\right)\right\}\right\}^* \tag{35}$$

where "*" is the conjugate.

After matching the defocusing effects caused by the RCMC and performing the azimuth FFT, we finally obtain the imaging result in the two-dimensional time domain as follows

$$\begin{aligned} S_{image}(t_r, t_a) &= IFFT_{f_a}\{S_7(t_r, f_a)\cdot H_{match}(t_r, f_a)\} \\ &= Asinc\left[B\left(t_r - \frac{2R_0}{c}\right)\right]sinc\left[\frac{4a_2 T_s}{\lambda}t_a\right] \end{aligned} \tag{36}$$

In the imaging result of the stationary scene without processing of GMTI, targets moving along the radial direction appear displaced in azimuth from their original position. The targets moving with radial velocity are shifted in azimuth by [1]

$$\Delta_{az} = -R\frac{v_r}{|v|} \tag{37}$$

where R is the distance from the sensor to the targets.

In the above analysis, the proposed method is derived in the scenario with a single target. However, it can also be extended to the scenario with multiple targets. Firstly, moving-target focusing imaging is carried out after clutter suppression and target detection. Therefore, we can separate the multiple targets according to their different moving trajectories. Moreover, if the scattering intensities of different targets differ significantly, the 'CLEAN' technique could be applied to eliminate the effect of the strong target [14,21]. In this way, the coherent integration of strong moving targets and weak ones can be achieved iteratively.

3.5. Computational Complexity Analysis

The computational complexity of four existing methods is compared to show that the proposed method has low computational complexity. N_r and N_a represent the number of range cells and the number of azimuth pulses, respectively. The searching times of a_1, a_2 and a_3 are the same, denoted by M, which is usually be larger than N_r and N_a [8,10,25].

The GRFT method [29] is considered a statistically optimal method. Its implementation mainly includes the 3D grid searching of target motion parameters [14,25,29], whose computational complexity is about $O\left(N_r N_a M^3\right)$. The 2D frequency matched filtering method [30] includes the searching of the second-order motion parameter with the computational complexity being about $O\left(M\left(N_r N_a \log_2^{N_r} + N_r N_a \log_2^{N_a}\right)\right)$. The Hough-GHAF [25] algorithm mainly includes a SOKT, a Hough transform to detect the line in range-time and azimuth-time domains, and a 1D search of a_2, whose total computational complexity is $O\left(N_r N_a^2 + M(M-1)N\right) + O\left(N_r N_a^2\right) + O\left(N_a^3\right) + O\left(M N_a \log_2^{N_a}\right)$ [8]. Concerning the KDCT-FSFT method [10], its major implementation procedures include the pre-filtering, KDCT for the RCMC, FSFT for the third-order Doppler parameter estimation and 2D-FFT, whose total computation is $O\left((N_a + M + 2)N_r N_a + (M+1)N_r N_a \log_2^{N_a} + N_r N_a \log_2^{N_r}\right)$.

The major implementation procedures of the proposed method include Hough transform with computational complexity of $O\left(N_r M^2\right)$, the pre-filtering with computational complexity of $O(N_r N_a)$, the SOKT for the range curvature correction with computational complexity [14] of $O\left((N_a+1)N_r N_a + N_r N_a \log_2^{N_r}\right)$, SAC for the third-order Doppler parameter estimation with computational complexity of $O\left(N_a + N_a \log_2^{N_a}\right)$ and 2D-FFT with computational complexity of $O\left(N_r N_a \log_2^{N_r} + N_r N_a \log_2^{N_a}\right)$. So, its total computational cost is

$$O\left(N_r M^2 + (N_a+2)N_r N_a + N_a + N_a \log_2^{N_a} + N_r N_a \log_2^{N_r} + N_r N_a \log_2^{N_a}\right) \tag{38}$$

Let $M = N_r = N_a = N$; the computational complexity of the five methods is listed in Table 1. It can be seen from Table 1 that the proposed method has the lowest computational complexity.

Table 1. Comparisons of computational complexity.

Methods	Computational Complexity
GRFT method [29]	$O\left(N^5\right)$
2-D frequency matched filtering [30]	$O\left(N^3 \log_2^N\right)$
Hough-GHAF method [25]	$O\left(4N^3 + N^2 \log_2^N\right)$
KDCT-FSFT method [10]	$O\left(2N^3 + N^3 \log_2^N\right)$
Proposed method	$O\left(2N^3 + N^2 \log_2^N\right)$

4. Algorithm Implementation

The proposed algorithm is designed to image raw data. So, clutter suppression, target detection and target signal extraction are necessary before refocusing moving targets. The flow chart is shown in Figure 4. The processing mainly includes clutter suppression, target detection and target signal extraction, target motion parameter estimation and focus imaging. The detailed processing process is as follows.

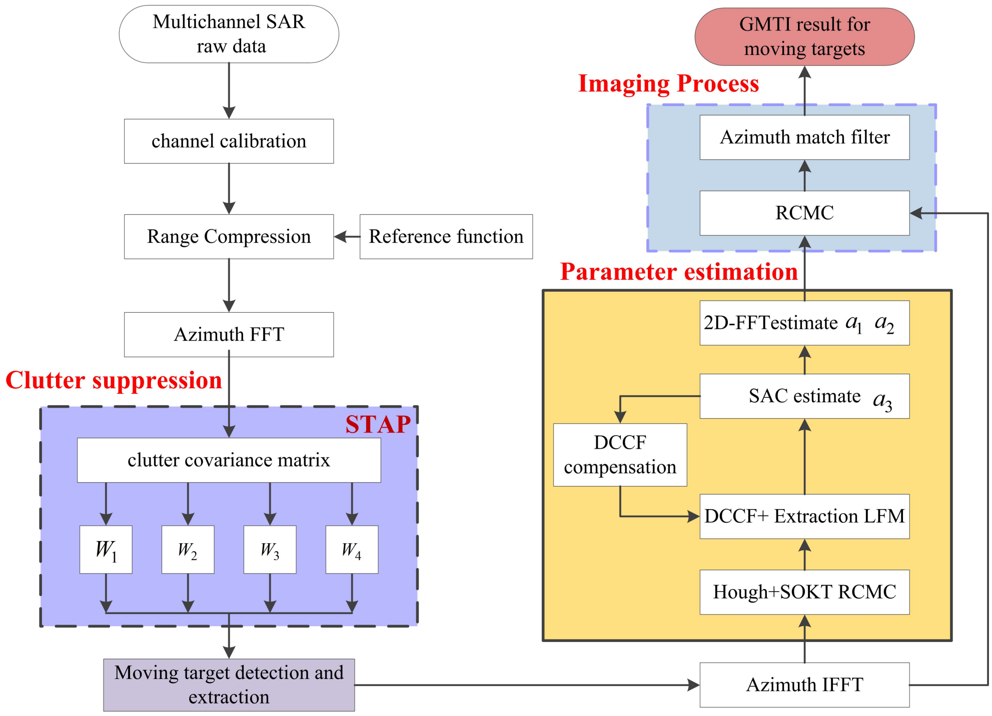

Figure 4. The flowchart of the proposed method.

Step 1: Clutter suppression and target signal extraction

Before imaging the moving target, we need to remove clutter in the signal by pretreatment. The moving-target signal is extracted after baseline delay compensation, channel equalization processing, STAP clutter suppression, and target detection operations on the multi-channel SAR signals. These pretreatments are shown in reference [31].

Step 2: RCMC

Hough transform and the SOKT are used to complete the range walk and the range curvature correction, so as to concentrate the signal energy into a range cell.

Step 3: Motion parameter estimation

A DCCF is constructed in the range-frequency domain and azimuth-time domain. An azimuth chirp signal is extracted at the cross-correlation peak range cell. The SAC algorithm is used to accurately estimate a_3, and the residual range migration is further corrected with a_3. Then, 2D-FFT transform is used to estimate the values of a_1 and a_2.

Step 4: Imaging Processing

The accurate range migration compensation function and the azimuth matched function are constructed according to the estimated $\widehat{a_1}$, $\widehat{a_2}$ and $\widehat{a_2}$ to obtain focused imaging and accurately position the moving targets.

Step 5: Target Relocation

After obtaining the precise motion parameters, we can correct the position of the target by Equation (37).

5. Experimental Results

In order to verify the focusing performance of the proposed method, two types of target simulation, single-point scattering and multi-point scattering, were carried out, and compared with KT-CICPF [9]. Finally, experimental results of airborne X-band SAR data are given.

5.1. Simulation Experiment

- **Point target**

Firstly, the effectiveness of the algorithm is verified by the simulation of a single scattering point target. The simulation parameters are shown in Table 2. At $t_a = 0$, the position of the target is at the center of the scene, and the coordinate is $P_0(0, 5000)$. This paper is mainly aimed at the ground vehicle target. In a synthetic aperture time, it can be considered that the motion characteristics of the scattering points of each part of the target are the same [32]; that is, the speed and acceleration of each part are the same, and there is no rotational motion. Rotating target detection and parameter estimation can be found in the literature [33,34].

Table 2. Simulation parameter.

Parameter	Value	Parameter	Value
Carrier frequency	10 GHz	Range sampling frequency	2000 MHz
Platform velocity	100 m/s	Pulse duration time	1 µs
Range bandwidth	1000 Mhz	Center slant range	5 Km
Pulse repetition frequency	1200 Hz	Synthetic aperture time	5 s
v_r	3 m/s	a_r	-1 m/s^2
v_x	4 m/s	a_x	2 m/s^2

The target trajectory after range compression is shown in Figure 5a. It can be seen from the figure that the target trajectory has serious range migration caused by the target movement. After Hough-SOKT and third-order term migration correction, the DCCF constructed by the proposed method is shown in Figure 5b, the target energy is corrected for the same range cell. However, the peak position of the DCCF constructed by KT-CICPF is shifted by the range cell, and its peak energy is dispersed into three range cells, as shown in Figure 5c. The reason for this problem is the coupling between DCCF and the range migration caused by insufficient range migration correction, which directly affects the extraction of the chirp signal of Equation (24). The DCCF after third-order correction is shown in Figure 5b. The amplitude and Doppler spectrum of $S_5(t_m)$ extracted by the two methods are shown as Figure 5d,e. It can be seen that the amplitude gain of the signal extracted by the proposed method is stronger and the Doppler spectrum is smoother, which conforms to the ideal chirped signal. However, the amplitude and Doppler spectrum extracted by KT-CICPF fluctuate greatly. Figure 5f,g show the F_0–F_1 parameter plane constructed by the two methods. Inside the red rectangle is a local magnification of the peak position. Figure 5h shows the slice along F_1 in the F_0–F_1 plane. It can be clearly seen that the peak of the parameter plane constructed by the proposed method is more significant, while the parameter plane generated by KT-CICPF is energy-dispersive. Figure 5i,j show the imaging results of the two methods, respectively. Figure 5k,l are slices of the imaging results in the range direction and azimuth direction. It can be seen from the figure that the proposed method has a better focus. However, in the contrasting method, the target occupies multiple range cells due to the residual range migration, which reduces the resolution of the target.

The parameter estimation results obtained by the two methods are shown in Table 3. It can be seen that the parameter estimation accuracy of the proposed method is relatively high, while the parameter error estimated by KT-CICPF is relatively large. Especially for the estimated value of a_2, the error of the KT-CICPF method reaches 7.01%, while the maximum relative error of the parameters estimated by the proposed method is only 0.21%. Therefore, it can be concluded that the proposed method has better parameter estimation performance.

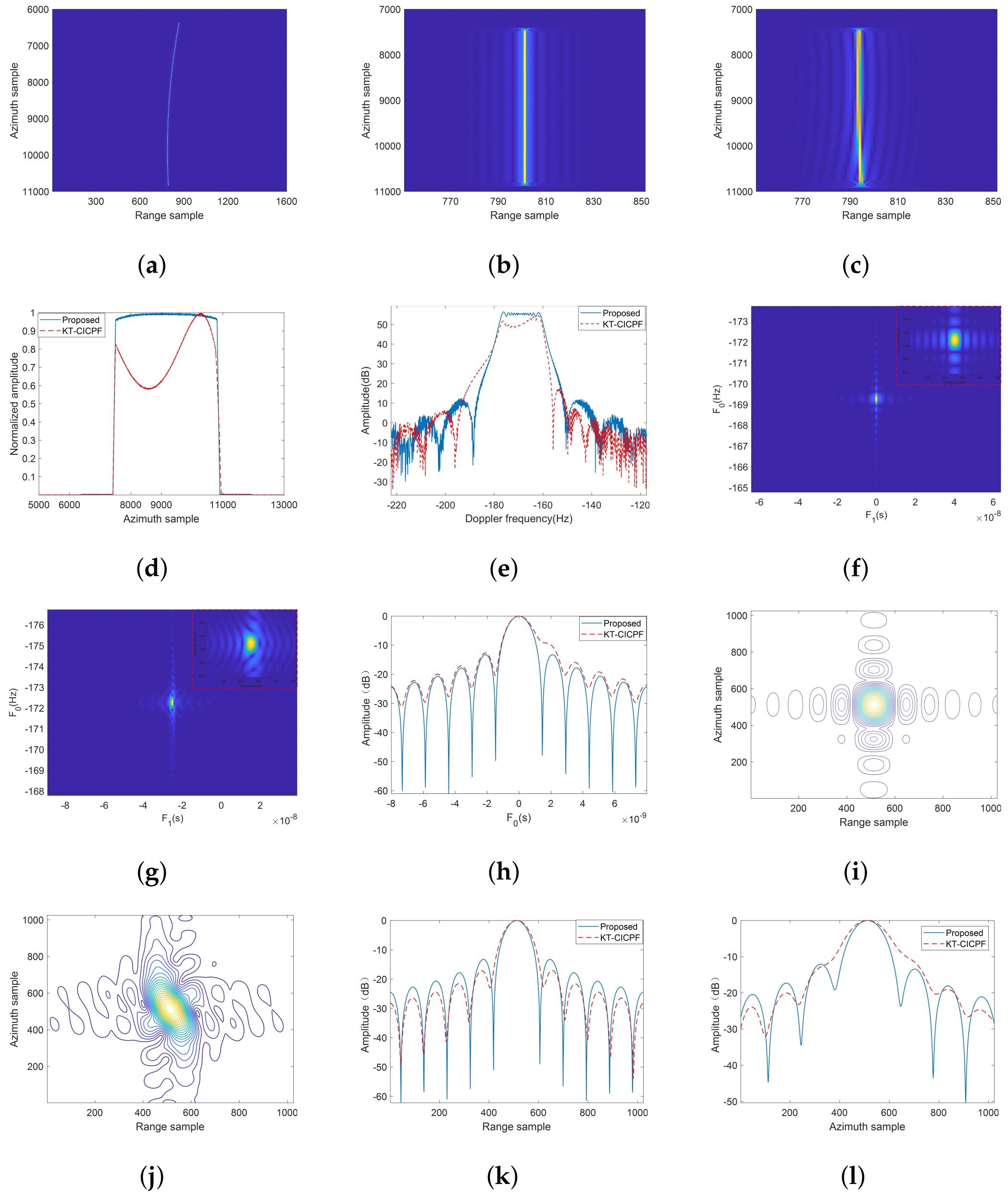

Figure 5. The focused images of point target. (**a**) Range compression. (**b**) The proposed DCCF. (**c**) DCCF constructed by KT-CICPF. (**d**) Peak signal extracted by DCCF. (**e**) Spectrum of peak signal. (**f**) F_0–F_1 parametric plane by proposed method. (**g**) F_0–F_1 1parametric plane by KT-CICPF. (**h**) F_0 slice. (**i**) Image of the proposed method (64× upsampling). (**j**) Image of the KT-CICPF method (64× upsampling). (**k**) Range slice (64× upsampling). (**l**) Azimuth slice (64× upsampling).

Table 3. The motion parameter estimation results of the point target obtained by the two methods.

Parameter	True	Proposed Method		KT-CICPF	
		Estimate	Erro%	Estimate	Erro%
a_1	−3.00000000	−2.99384938	0.20502050	−3.01689870	0.56329000
a_2	1.42160000	1.42090117	0.04915745	1.32186099	7.01596862
a_3	−0.01864704	−0.01868167	0.18571902	−0.01828961	1.916818969

In addition, the focusing performance of the moving target is shown in Table 4. The theoretical range resolution is $0.886(c/2B) = 0.1329$ m. According to Equation (5), the Doppler bandwidth of the moving target in the synthetic aperture time can be calculated. So, the theoretical azimuth resolution is $0.886(v/B_a) = 0.1256$ m. As can be seen from the table, the resolution obtained by the proposed method is closer to the theoretical value than that obtained by KT-CICPF method. The azimuth resolution of the KT-CICPF method has a maximum broadening of about 26.51%. The theoretical values of the peak sidelobe ratio (PSLR) and integrated sidelobe ratio (ISLR) are −13.27 and −10.24 dB [10]. For the proposed method, the range and azimuth PSLR/ISLR values have small deviations from the theoretical values. Figure 5i,j show the imaging results of the two methods, respectively. Figure 5k,l are slices of the imaging results in the range direction and azimuth direction. It can be seen that the proposed method has a better focusing performance.

Table 4. Focuing Performance.

Method	Parameter	Resolution (m)	PSLR (dB)	ISLR (dB)
Theoretical value	Range	0.1329	−13.27	−10.24
	Azimuth	0.1256	−13.27	−10.24
Proposed method	Range	0.1338	−13.26	−10.21
	Azimuth	0.1288	−12.05	−9.70
KT-CICPF	Range	0.1463	−17.03	−14.46
	Azimuth	0.1589	−18.77	−16.66

- **Distributed Target**

In high-resolution SAR images, the target is often composed of multiple pixels. In order to verify the ability of the algorithm to maintain the target geometry, this paper carried out the simulation analysis of moving targets with "cross" distribution (hereinafter referred to as T1) and "circular" distribution (hereinafter referred to as T2). T1 consists of 15 strong scattering points. The azimuth and range intervals between the scattering points are both 0.5 m, and the coordinate distribution is shown in Figure 6a, where the red squares represent the positions of the scattering points. T2 is composed of 63 scattering points uniformly distributed on the circumference, and its coordinate distribution is shown in Figure 6b. In Figure 6, the abscissa is the slant range, and the ordinate is the azimuth coordinate.

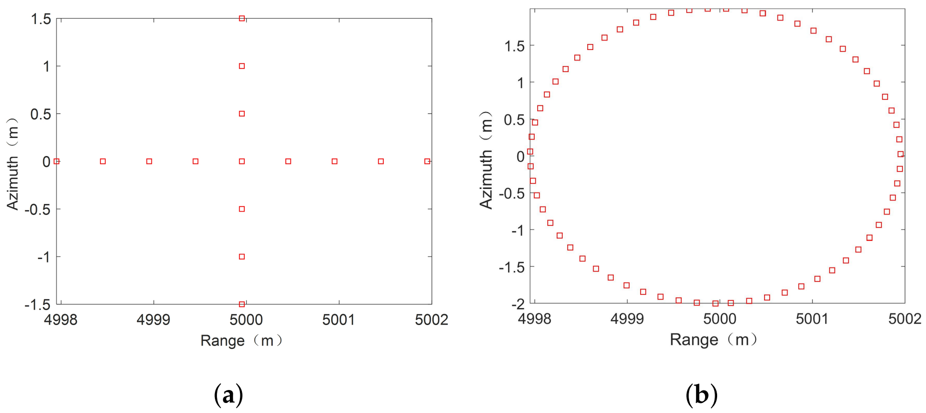

Figure 6. Scattering point coordinate distribution. (**a**) Scatters coordinate distribution of T1. (**b**) Scatters coordinate distribution of T2.

Two methods are used to process it. Figures 7 and 8 show the processing results of T1 and T2, respectively. Figures 7a,d and 8a,d are the amplitude and spectrum of the chirp signal corresponding to the DCCF peak range cell, which are used to estimate the coefficient of the third-order term. The signal gain and resolution extracted in the proposed method are higher than those extracted by KT-CICPF. Figure 8b,e are the F_0–F_1 parameter planes constructed by the two methods for the target T2, respectively. From the figures, it can be seen that the peak in the F_0–F_1 plane constructed by the proposed method is relatively concentrated and the coupling degree with range migration is small. The peak of the F_0–F_1 plane constructed by the KT-CICPF is divergent. The reason for this phenomenon is that the residual range migration by the KT-CICPF method is larger, resulting in a large parameter estimation error. For the target T1, Figure 8b,e illustrates the same phenomenon. In this paper, when constructing the F_0–F_1 plane, Equation (29) is used to compensate for the DCCF to reduce the influence of the third-order range migration on the F_0–F_1 parameter plane. Figures 7c,f and 8c,f show refocused results of the two methods. It can be seen that the imaging results of KT-CICPF methods are severely defocused in azimuth. The proposed method can better maintain the shape of the target.

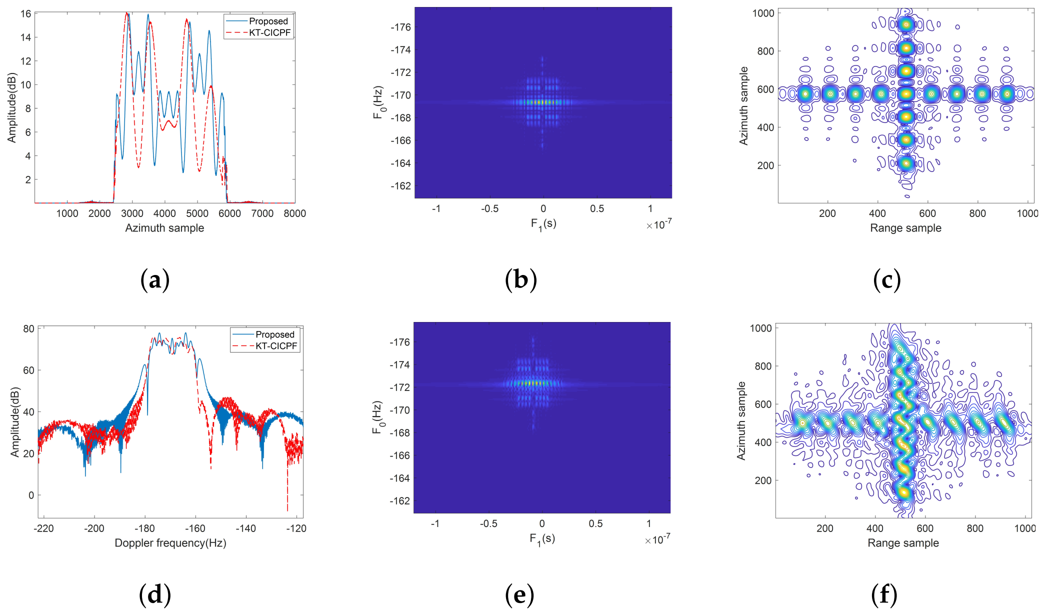

Figure 7. The focused images of T1. (**a**) Peak signal extracted by DCCF. (**b**) F_0–F_1 parametric plane by proposed method. (**c**) Imaging by proposed method (16× upsampling). (**d**) Spectrum of peak signal. (**e**) F_0–F_1 parametric plane by KT-CICPF. (**f**) Imaging by KT-CICPF (16× upsampling).

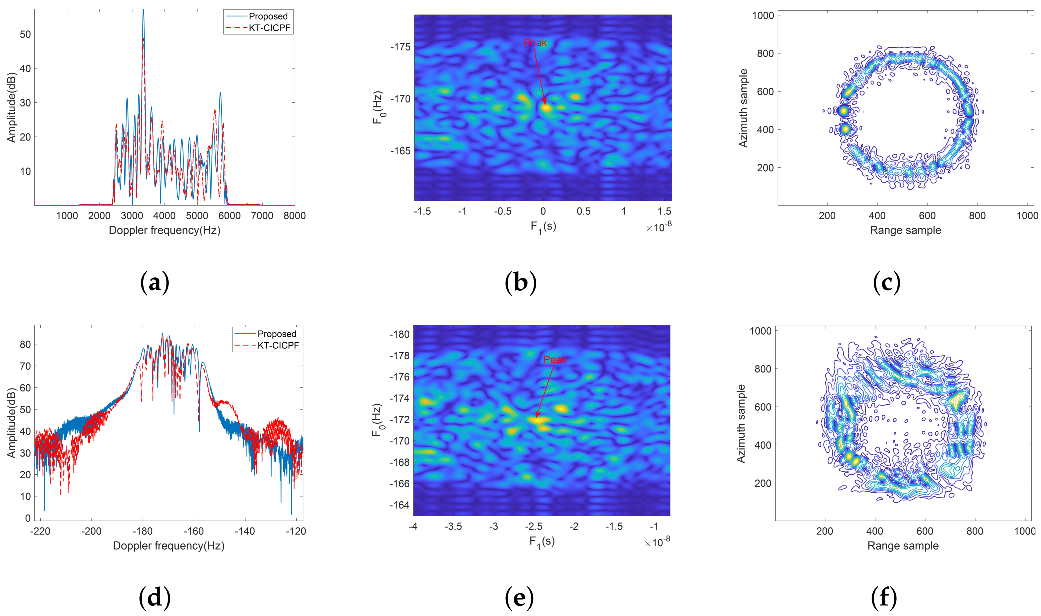

Figure 8. The focused images of T2. (**a**) Peak signal extracted by DCCF. (**b**) F_0–F_1 parametric plane by proposed method. (**c**) Imaging by proposed method (16× upsampling). (**d**) Spectrum of peak signal. (**e**) F_0–F_1 parametric plane by KT-CICPF. (**f**) Imaging by KT-CICPF (16× upsampling).

5.2. Measured Experiment

In this paper, the real data collected by a four-channel airborne X-band SAR system are used to verify the performance of the proposed method. The system parameters are shown in Table 5. The four channels are equally spaced in the azimuth direction, and the working mode of one-transmitter and four-receiver is adopted. In this paper, the target signal extracted after clutter suppression is imaged. The flight platform and cooperation targets are shown in Figure 9a,b, respectively. There are three electric tricycles as cooperative targets in the experiment. Each target is equipped with a corner reflector, and a GPS device is installed to record the real-time position and speed information of the target as the true value of the target movement.

Table 5. The parameters of X-band airborne SAR system.

Parameter	Value	Parameter	Value
Wave band	X	Pulse duration time	5 μs
Range bandwidth	1800 MHz	Pulse repetition frequency	2000 Hz
Range sampling frequency	2000 MHz	Center slant range	7 Km
Target velocity	<3 m/s	Synthetic aperture time	5 s

(**a**) (**b**)

Figure 9. Flying platform and cooperation targets. (**a**) Flying platform. (**b**) Cooperation targets.

The imaging result of the stationary scene without processing of GMT is shown in Figure 10a. The magnified images of T1–T3 are shown in Figure 10b–d, respectively. As can be seen from the figure, targets moving along the radial direction are defocused and appear displaced in azimuth from their original position.

Taking the target T1 as an example, the processing results of each step of the proposed method are analyzed. The target signal after clutter suppression is shown in Figure 11a. Figure 11b,c are the two-dimensional time domain signal and range-Doppler domain signal after RCMC, respectively. It can be seen that the target energy is basically corrected to the same range cell after Hough-SOKT. Figure 11d is the F_0–F_1 parameter plane constructed by the proposed method, and Figure 11e is the slice along F_0 at the peak of the parameter plane obtained by the two methods. Obviously, the peak value obtained by the proposed method is larger, which verifies that the proposed method can can obtain higher coherent accumulation gain. Figure 11f,g show the refocused results of T1 by two methods, the proposed method has better focusing. Figure 11h,i are slices in the range and azimuth directions, from which it can be seen that the focusing of the target in the azimuth has been significantly improved. In Figure 11f–i, the image is interpolated 16-fold in azimuth and range directions. The results verify that a better focusing performance can be obtained by the proposed method.

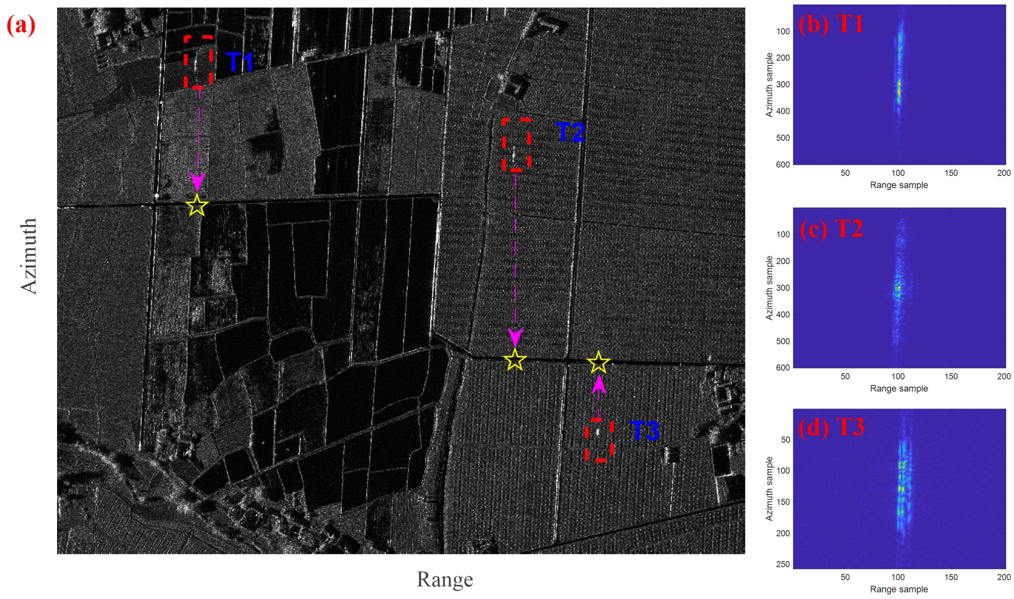

Figure 10. Image of the stationary scene without processing of GMT. (**a**) Image of the stationary scene (the yellow pentagram indicates the target's relocation position). (**b**–**d**) Magnified images of moving targets (defocused).

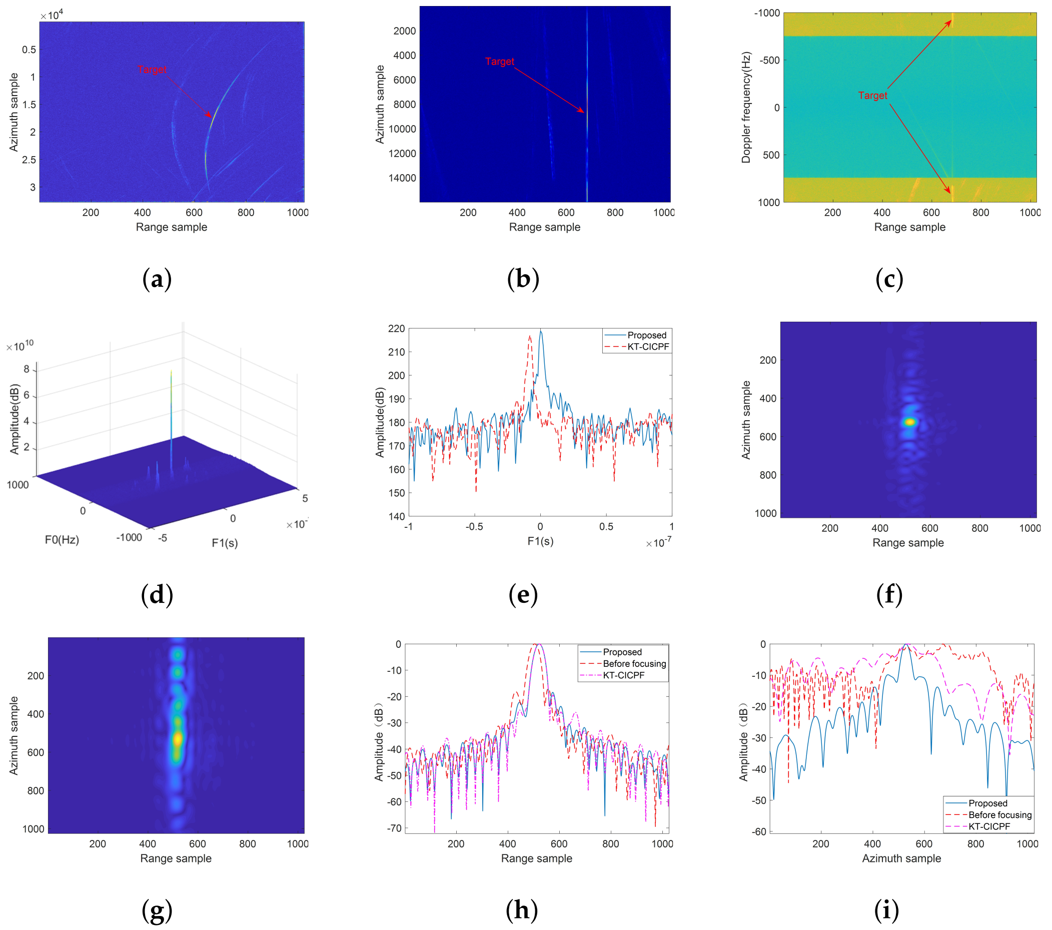

Figure 11. Processing result of T1. (**a**) Target signal after clutter suppression. (**b**) Hough+SOKT RCMC; (**c**) Range-Doppler domain. (**d**) F_0–F_1 parametric plane. (**e**) F_0 estimate. (**f**) Imaging by proposed method (16× upsampling). (**g**) Imaging by KT-CICPF (16× upsampling). (**h**) Slice in range. (**i**) Slice in azimuth.

To verify the adaptability of the algorithm, the same processing is used for T2 and T3 as for T1. Figure 12 shows the refocused results of the three targets by three methods. The magnified images of moving targets without processing of GMT are shown in Figure 12a–c, respectively. The refocused results by the KT-CICPF method of T1–T3 are shown in Figure 12d–f. The results by the proposed method are given in Figure 12g–i. As can be seen from the figure, the focusing effect of the proposed method on T1–T3 is superior to that of KT-CICPF method.

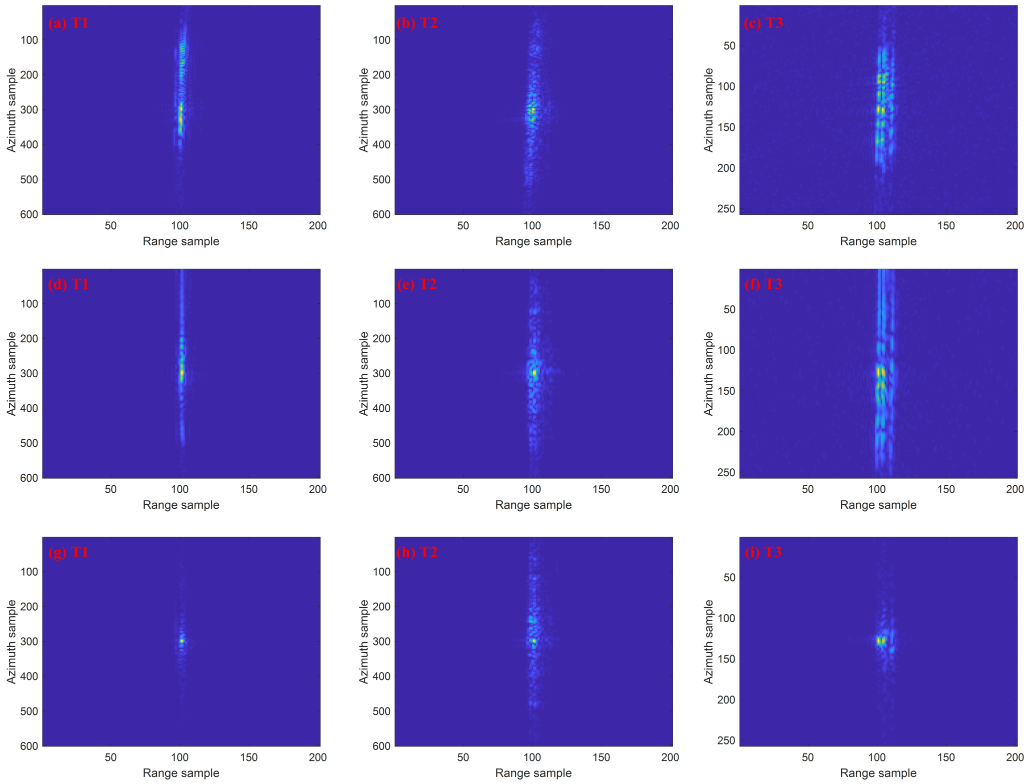

Figure 12. Moving-target focus results. (**a**–**c**) Magnified images of moving targets without processing of GMT (defocused). (**d**–**f**) Refocused results by KT-CICPF. (**g**–**i**) Refocused results by proposed method.

In addition, the focusing performance of the moving target is shown in Table 6. The theoretical range resolution is $0.886(c/2B) = 0.0738$ m. According to the system parameters, the Doppler bandwidth in the synthetic aperture time is about 300 Hz. So, the theoretical azimuth resolution is $0.886(v/B_a) = 0.2017$ m. As can be seen from the table, the resolution obtained by the proposed method is closer to the theoretical value than that obtained by the KT-CICPF method. The azimuth resolution of the KT-CICPF method has a greater broadening. It is proved that the proposed method has better focusing performance.

Table 6. The Resolution of measured data.

Target	Resolution (m)	Proposed Method	KT-CICPF
T1	Range	0.0918	0.0913
	Azimuth	0.2317	0.6078
T2	Range	0.0926	0.0924
	Azimuth	0.2590	0.4479
T3	Range	0.0867	0.0824
	Azimuth	0.2143	0.3383

The radial velocities of T1–T3 estimated by the proposed method are 1.3156 m/s, 1.6851 m/s and −0.5725m/s, respectively. The distances of the three targets to the sensor are 7339.3228 m, 7631.5370 m and 7736.4643. In accordance with Equation (37), the three targets are shifted in azimuth by 140.7934 m, 187.5168 m and −64.5833 m, respectively. After azimuth shift correction, the positions of the three targets are indicated by pentagrams in Figure 10a. The targets are basically positioned on the road. The accuracy of the estimated parameters is verified again.

6. Conclusions

This paper proposed an improved ground moving-target parameter estimation and imaging method for multichannel high-resolution SAR. The proposed method constructs the DCCF after the RCMC and compensates the residual range migration with the estimated third-order terms, which can reduce the coupling degree between the peak position of DCCF and the target range migration. The proposed method can obtain the DCCF with a higher integral gain, which ensures the performance of parameter estimation. In addition, the process of parameter estimation is simplified to peak detection by the SAC algorithm and 2D-FFT, avoiding parameter search. Compared with the existing methods, the proposed method has a better focusing effect and lower computational complexity. Finally, simulation and measured data are given to verify the effectiveness of the proposed method.

Author Contributions: All authors have made contributions to the article in different areas. Conceptualization, B.W., M.X. and Z.W.; Investigation, Q.D.; Software, Q.D.; Writing—original draft preparation, Z.W.; Writing—review & editing, Z.W., Z.J. and C.S. All authors have read and agreed to the published version of the manuscript.

Funding: This work was supported by the National Natural Science Foundation of China under Grant No. 62073306 and Grant No. 61991424. This work was also supported by the Youth Innovation Promotion Association CAS.

Institutional Review Board Statement: Not applicable.

Informed Consent Statement: Not applicable.

Data Availability Statement: Data sharing not applicable.

Acknowledgments: The authors would like to thank the staff of the National Key Laboratory of Microwave Imaging Technology, Aerospace Information Research Institute, Chinese Academy of Sciences, for their valuable conversations and comments.

Conflicts of Interest: The authors declare no conflict of interest.

References

1. Budillon, A.; Gierull, C.H.; Pascazio, V.; Schirinzi, G. Along-Track Interferometric SAR Systems for Ground-Moving Target Indication: Achievements, Potentials, and Outlook. *IEEE Geosci. Remote Sens. Mag.* **2020**, *8*, 46–63. [CrossRef]
2. Huang, P.; Zhang, X.; Zou, Z.; Liu, X.; Liao, G.; Fan, H. Road-Aided Along-Track Baseline Estimation in a Multichannel SAR-GMTI System. *IEEE Geosci. Remote Sens. Lett.* **2021**, *18*, 1416–1420. [CrossRef]
3. Gierull, C.H. Closed-Form Expressions for InSAR Sample Statistics and Its Application to Non-Gaussian Data. *IEEE Trans. Geosci. Remote Sens.* **2021**, *59*, 3967–3980. [CrossRef]
4. Wang, W.; An, D.; Luo, Y.; Zhou, Z. The Fundamental Trajectory Reconstruction Results of Ground Moving Target From Single-Channel CSAR Geometry. *IEEE Trans. Geosci. Remote Sens.* **2018**, *56*, 5647–5657. [CrossRef]
5. Li, Y.; Wang, Y.; Liu, B.; Zhang, S.; Nie, L.; Bi, G. A New Motion Parameter Estimation and Relocation Scheme for Airborne Three-Channel CSSAR-GMTI Systems. *IEEE Trans. Geosci. Remote Sens.* **2019**, *57*, 4107–4120. [CrossRef]
6. Zhang, X.; Yang, C.; Lin, Q.; Zhang, X. Efficient Parameters Estimation Methods for Radar Moving Targets Without Searching. *IEEE Access* **2020**, *8*, 41351–41361. [CrossRef]
7. Lan, Y.; Li, Z.; Qu, J.; Wu, J.; Yang, J. A Fast Doppler Parameters Estimation Method for Moving Target Imaging Based ON 2D-FFT. In Proceedings of the IGARSS 2018—2018 IEEE International Geoscience and Remote Sensing Symposium, Valencia, Spain, 22–27 July 2018; pp. 589–592. [CrossRef]
8. Zeng, C.; Li, D.; Luo, X.; Song, D.; Liu, H.; Su, J. Ground Maneuvering Targets Imaging for Synthetic Aperture Radar Based on Second-Order Keystone Transform and High-Order Motion Parameter Estimation. *IEEE J. Sel. Top. Appl. Earth Obs. Remote Sens.* **2019**, *12*, 4486–4501. [CrossRef]
9. Huang, P.; Xia, X.G.; Liao, G.; Yang, Z. Ground Moving Target Imaging Based on Keystone Transform and Coherently Integrated CPF With a Single-Channel SAR. *IEEE J. Sel. Top. Appl. Earth Obs. Remote Sens.* **2017**, *10*, 5686–5694. [CrossRef]

10. Liu, Z.; Li, Z.; Huang, C.; Wu, J.; Yang, J. Bistatic Forward-Looking SAR KDCT-FSFT-Based Refocusing Method for Ground Moving Target With Unknown Curve Motion. *IEEE J. Sel. Top. Appl. Earth Obs. Remote Sens.* **2020**, *13*, 4848–4858. [CrossRef]
11. Ran, L.; Liu, Z.; Zhang, L.; Xie, R.; Li, T. Multiple Local Autofocus Back-Projection Algorithm for Space-Variant Phase-Error Correction in Synthetic Aperture Radar. *IEEE Geosci. Remote Sens. Lett.* **2016**, *13*, 1241–1245. [CrossRef]
12. Hui, Z.; Fengjun, Z.; Jian, Y. SAR Accelerating Moving Target Parameter Estimation and Imaging Based on Three-order Polynomial Fourier Transform. *J. Electron. Inf. Technol.* **2016**, *38*, 8. [CrossRef]
13. Cristallini, D.; Pastina, D.; Colone, F.; Lombardo, P. Efficient Detection and Imaging of Moving Targets in SAR Images Based on Chirp Scaling. *IEEE Trans. Geosci. Remote Sens.* **2013**, *51*, 2403–2416. [CrossRef]
14. Kong, L.; Li, X.; Cui, G.; Yi, W.; Yang, Y. Coherent Integration Algorithm for a Maneuvering Target With High-Order Range Migration. *IEEE Trans. Signal Process.* **2015**, *63*, 4474–4486. [CrossRef]
15. Mu, H.; Zhang, Y.; Ding, C.; Jiang, Y.; Er, M.H.; Kot, A.C. DeepImaging: A Ground Moving Target Imaging Based on CNN for SAR-GMTI System. *IEEE Geosci. Remote Sens. Lett.* **2021**, *18*, 117–121. [CrossRef]
16. Fienup, J. Detecting moving targets in SAR imagery by focusing. *IEEE Trans. Aerosp. Electron. Syst.* **2001**, *37*, 794–809. [CrossRef]
17. Perry, R.; DiPietro, R.; Fante, R. SAR imaging of moving targets. *IEEE Trans. Aerosp. Electron. Syst.* **1999**, *35*, 188–200. [CrossRef]
18. Huang, P.; Xia, X.G.; Liao, G.; Yang, Z.; Zhou, J.; Liu, X. Ground Moving Target Refocusing in SAR Imagery Using Scaled GHAF. *IEEE Trans. Geosci. Remote Sens.* **2018**, *56*, 1030–1045. [CrossRef]
19. Yang, J.; Zhang, Y. An Airborne SAR Moving Target Imaging and Motion Parameters Estimation Algorithm With Azimuth-Dechirping and the Second-Order Keystone Transform Applied. *IEEE J. Sel. Top. Appl. Earth Obs. Remote Sens.* **2015**, *8*, 3967–3976. [CrossRef]
20. Tang, X.; Zhang, X.; Shi, J.; Wei, S. A Novel Ground Moving Target Radial Velocity Estimation Method for Dual-Beam Along-Track Interferometric Sar. In Proceedings of the IGARSS 2020—2020 IEEE International Geoscience and Remote Sensing Symposium, Waikoloa, HI, USA, 26 September–2 October 2020; pp. 389–392. [CrossRef]
21. Tian, J.; Cui, W.; Xia, X.G.; Wu, S.L. Parameter Estimation of Ground Moving Targets Based on SKT-DLVT Processing. *IEEE Trans. Comput. Imaging* **2016**, *2*, 13–26. [CrossRef]
22. Chao, W.; Yanfei, W.; Chang, L.; Bidan, L. A New Approach to Range Cell Migration Correction for Ground Moving Targets in High-resolution SAR System Based on Parameter Estimation. *J. Radars* **2019**, *8*, 64–72. [CrossRef]
23. Zhang, X.; Liao, G.; Zhu, S.; Yang, D.; Xu, J. A geometry-based hough transform estimation for radial velocity of moving target using single antenna SAR. In Proceedings of the 2014 XXXIth URSI General Assembly and Scientific Symposium (URSI GASS), Beijing, China, 16–23 August 2014; pp. 1–4. [CrossRef]
24. Chen, S.; Yuan, Y.; Zhang, S.; Zhao, H.; Chen, Y. A New Imaging Algorithm for Forward-Looking Missile-Borne Bistatic SAR. *IEEE J. Sel. Top. Appl. Earth Obs. Remote Sens.* **2016**, *9*, 1543–1552. [CrossRef]
25. Huang, P.; Liao, G.; Yang, Z.; Xia, X.G.; Ma, J.; Zheng, J. Ground Maneuvering Target Imaging and High-Order Motion Parameter Estimation Based on Second-Order Keystone and Generalized Hough-HAF Transform. *IEEE Trans. Geosci. Remote Sens.* **2017**, *55*, 320–335. [CrossRef]
26. Wu, Y.-F.; Sun, G.-C.; Xing, M.-D.; Bao, Z. An Improved Doppler Rate Estimation Approach Based on the Range-Keystone Transform. *J. Electron. Inf. Technol.* **2013**, *35*, 7. [CrossRef]
27. Liao, Y.; Wang, W.Q.; Liu, Q.H. Two-Dimensional Spectrum for Circular Trace Scanning SAR Based on an Implicit Function. *IEEE Geosci. Remote Sens. Lett.* **2016**, *13*, 887–891. [CrossRef]
28. Wang, R.; Deng, Y.K.; Loffeld, O.; Nies, H.; Walterscheid, I.; Espeter, T.; Klare, J.; Ender, J.H.G. Processing the Azimuth-Variant Bistatic SAR Data by Using Monostatic Imaging Algorithms Based on Two-Dimensional Principle of Stationary Phase. *IEEE Trans. Geosci. Remote Sens.* **2011**, *49*, 3504–3520. [CrossRef]
29. Xu, J.; Xia, X.G.; Peng, S.B.; Yu, J.; Peng, Y.N.; Qian, L.C. Radar Maneuvering Target Motion Estimation Based on Generalized Radon-Fourier Transform. *IEEE Trans. Signal Process.* **2012**, *60*, 6190–6201. [CrossRef]
30. Zhu, S.; Liao, G.; Yang, D.; Tao, H. A New Method for Radar High-Speed Maneuvering Weak Target Detection and Imaging. *IEEE Geosci. Remote Sens. Lett.* **2014**, *11*, 1175–1179. [CrossRef]
31. Dong, Q.; Wang, B.; Xiang, M.; Wang, Z.; Wang, Y.; Song, C. A Novel Detection Scheme in Image Domain for Multichannel Circular SAR Ground-Moving-Target Indication. *Sensors* **2022**, *22*, 2596. [CrossRef]
32. Liu, B.; Yin, K.; Li, Y.; Shen, F.; Bao, Z. An Improvement in Multichannel SAR-GMTI Detection in Heterogeneous Environments. *IEEE Trans. Geosci. Remote Sens.* **2015**, *53*, 810–827. [CrossRef]
33. Fu, K. Aircraft Reconstruction in High-Resolution SAR Images Using Deep Shape Prior. *ISPRS Int. J. Geo-Inf.* **2017**, *6*, 330. [CrossRef]
34. Zibo, Z.; Chaowei, Z.; Saiqiang, X. Feature Extraction of Rotor Blade Targets Based on Phase Compensation in a Passive Bistatic Radar. *J. Radars* **2021**, *10*, 15. [CrossRef]